

Stressed Volume Estimated by Finite Element Analysis Predicts the Fatigue Life of Human Cortical Bone: The Role of Vascular Canals as Stress Concentrators

^{a,b}Loundagin, L.L., ^aPohl, A.J., ^{a,b}Edwards, W.B.

^aHuman Performance Laboratory, Faculty of Kinesiology, University of Calgary

^bMcCaig Institute for Bone and Joint Health, Cumming School of Medicine, University of Calgary

ABSTRACT

The fatigue life of cortical bone can vary several orders of magnitude, even in identical loading conditions. A portion of this variability is likely related to intracortical microarchitecture and the role of vascular canals as stress concentrators. The size, spatial distribution, and density of canals determine the peak magnitude and volume of stress concentrations. This study utilized a combination of experimental fatigue testing and image-based finite element (FE) analysis to establish the relationship between the stressed volume (i.e., volume of bone above yield stress) associated with vascular canals and the fatigue life of cortical bone. Thirty-six cortical bone samples were prepared from human femora and tibiae from five donors. Samples were allocated to four loading groups, corresponding to stress ranges of 60, 70, 80, and 90 MPa, then cyclically loaded in zero-compression until fracture. Porosity, canal diameter, canal separation, and canal number for each sample was quantified using X-ray microscopy (XRM) after testing. FE models were created from XRM images and used to calculate the stressed volume. Stressed volume was a good predictor of fatigue life, accounting for 67% of the scatter in fatigue-life measurements. An increase in stressed volume was most strongly associated with higher levels of intracortical porosity and larger canal diameters. The findings from this study suggest that a large portion of the fatigue-life variance of cortical bone in zero-compression is driven by intracortical microarchitecture, and that fatigue failure may be predicted by quantifying the stress concentrations associated with vascular canals.

INTRODUCTION

Fatigue fractures, such as stress fractures and insufficient fractures, are common injuries resulting from the repetitive loading of weight bearing bones. The pathophysiology of fatigue fracture is consistent with a mechanical fatigue phenomenon, in which repetitive loading causes the accumulation of microdamage that may eventually lead to fracture at loading magnitudes well below the bone's monotonic ultimate strength [1,2]. Biomechanics research often relies on apparent-level estimations of stress to assess the risk of stress fracture [3,4]; however, like most engineering materials, the mechanical fatigue behavior of cortical bone is a stochastic process. Even when peak apparent stress is held constant, fatigue-life measurements (i.e., the number of loading cycles to failure) exhibit a large degree of scatter, which can vary more than two orders of magnitude [5,6]. Previous research has demonstrated that both material properties and loading conditions have a considerable influence on the fatigue life of bone [6–12]; however, beyond simple measures of porosity, very few studies have investigated the role of intracortical microarchitecture [13–15].

Intracortical microarchitecture plays a significant role in the extrinsic toughening mechanisms of cortical bone [16]. Osteons provide barriers to propagating cracks and the deflection of a crack around an osteon can increase bone toughness by up to 50% [17], which may explain why a higher osteonal density is related to a longer fatigue life [14]. However, in the absence of osteonal structure, plexiform bone has a longer fatigue life than secondary osteonal bone [13], suggesting that the increased porosity associated with osteonal remodeling may outweigh the toughening benefits of osteons. Recent studies have confirmed the negative effects of porosity on fatigue behavior in human cortical bone, in which increased porosity and larger canal diameters were

strongly associated with a shorter fatigue life [8,15]. Vascular canals, the primary contributor to intracortical porosity, act as stress concentrators in the bone matrix that may facilitate the initiation and propagation of microcracks [18,19]. Fatigue failures almost always occur in the presence of stress concentrations [20], and therefore, quantifying the stress concentrations associated with vascular canals may lead to more accurate predictions of fatigue life.

The extent to which stress concentrations diminish a material's strength is a function of both the magnitude and gradient of the surrounding stress field. According to the Theory of Critical Distances (TCD), failure will occur when the average stress over a critical distance from the stress concentration reaches a material-specific threshold (e.g., the yield stress) [21]. The stress gradient of a stress concentration is dependent on feature size (i.e., canal diameter), while the stress magnitude is not. Given the same shape and orientation, a smaller canal will induce a steeper stress gradient than a larger canal, and therefore, subject a smaller volume of bone to elevated stress. The TCD relies on linear-elastic finite element analysis to quantify the surrounding stress field, and has been shown to accurately predict fatigue failure for material's with a single stress concentration feature, such as a short crack or notch [22,23]. Similar to the critical stress estimated using the TCD approach, the total stressed volume (i.e., the volume of material above yield stress) quantifies the surrounding stress field, but may be a more practical measure for materials that contain multiple stress concentrations from more complex geometries.

The fatigue life of cortical bone is primarily determined by the applied stress range [10,12]. Normalizing stress range by elastic modulus, which is analogous to the initial strain range, reduces the scatter in fatigue life because of its dependence on tissue composition and porosity [24]. On the other hand, normalized stress does not account for the potential influence of stress concentrations associated with vascular canals. The primary purpose of this study was to determine if stressed volume can predict the fatigue life of human cortical bone in zero-compression across different stress ranges. Our secondary aim was to establish the relationship between stressed volume and intracortical microarchitecture, specifically the size, number, and spatial distribution of vascular canals. We hypothesized that stressed volume would better explain fatigue life variation than stress range and normalized stress range, and that increased stressed volume would be associated with larger and more abundant vascular canals.

METHODS

Sample Preparation

Thirty-six cortical bone samples from the mid-diaphysis of tibiae or femora were prepared from five cadaveric donors obtained through the University of Calgary's Body Donation Program and the Southern Alberta Tissue Program. Demographic information and cause of death for each donor are summarized in Table 1. The samples were comprised of cylindrical cores oriented along the longitudinal axis of the bone, approximately 35 mm in length and 5 mm in diameter extracted at random from all regions of the cortex. The exact dimensions and weight of each core were recorded for apparent density calculation. Each core was then turned down to a waisted geometry using a mini lathe (KC-0712ML, King Canada, Dorval, Québec); the central gauge length, gauge diameter, and transitional radius of the samples were 7, 2.5, and 5.5 mm, respectively. Samples were then hydrated with phosphate buffered saline (PBS) and stored in a -30°C freezer prior to mechanical testing.

Mechanical Testing

Samples were thawed and rehydrated in a PBS bath at room temperature for a minimum 6 hours before mechanical testing. Wedge grips (2742-206, Instron) with vee-serrated jaw faces (2703-803, Instron) were then used to secure the samples to an Instron Electropuls E3000 test frame (Instron, Norwood, MA). The initial elastic modulus (E^*) was quantified prior to fatigue testing with

an extensometer (632.29F-30, MTS, Eden Prairie, MN) mounted to the sample within the gauge region. A compressive preload of 100 N was first applied, followed by a ramped compressive load to 200 N corresponding to a stress of approximately 40 MPa. Elastic modulus was calculated from this initial test as the slope of the stress-strain curve over the entirety of the ramp load. The extensometer was then removed, and the samples were wrapped in PBS-soaked gauze.

After ensuring a balanced representation from each donor, samples were randomly allocated to four loading groups corresponding to a stress range of 60, 70, 80, and 90 MPa. Assuming an elastic modulus of 20 GPa, these loads corresponded to a strain of 3,000 to 4,500 $\mu\epsilon$, which is consistent with estimates of peak compressive tibial strains during running [3,4]. Cyclic compressive loads between 60 and 90 MPa have been shown to demonstrate fatigue failure within 10^1 - 10^6 cycles [7,8,15,25], enabling the evaluation of both low- and high-cycle fatigue behavior. The samples' cross-sectional area was used to scale the applied load such that the stress range of the sinusoidal waveform was consistent with the pre-determined stress range of the respective loading group. Samples were cyclically loaded in zero-compression at a frequency of 2 Hz at room temperature and under continuous PBS hydration. Fatigue life (N_f) was defined as the number of loading cycles until failure (i.e., complete fracture). If the sample lasted one million cycles it was considered to have 'run-out' and the test was terminated.

Quantifying microarchitecture and mineralization

A region of interest (ROI), 3 mm in height, was imaged using X-ray microscopy (Xradia Versa 520, Oberkochen, Germany) after testing. The position of the ROI was selected to be as close to the fracture surface as possible but only included regions with an uncompromised cross-section (i.e., full circular cross-sectional area). The isotropic voxel resolution was 3 μm and the scans were acquired using an objective of 0.4x, a 0.03 mm glass filter (LE1), a voltage of 70kV and power of 6W. Five-frame averaging was used to collect a total of 1014 images with an exposure time of 1 second, resulting in an overall scan time of approximately 1.5 hours.

To maintain consistency across all samples, a central ROI 2.5 mm in height and 2.5 mm in diameter, was used in the microstructural and finite element (FE) analyses (described below). The degree of mineralization and heterogeneity throughout the bone matrix was quantified as the mean and standard deviation, respectively, of grey scale values over the entire ROI. Vascular microarchitecture was segmented and quantified using the Fiji software package (v1.51, NIH, USA) [26]. Images were binarized using Fiji's built-in 'make binary' command, which implements an iterative process to select a histogram-based threshold and segment the image into bone and canal space. Porosity was calculated as the fraction of void volume to bone volume. Canal diameter (Ca.Dm) and canal separation (Ca.Sp) were determined using the thickness and separation options included in the BoneJ plugin [27]. The images were then filtered using BoneJ's purify function to retain only the largest connected canal network. This purified image was skeletonized and canal number (Ca.N) was calculated as one plus the number of junctions in the skeleton.

Finite element modeling

The FE models were generated and solved using FAIM software (v8.0, Numerics88 Solutions Ltd, Canada). Images were coarsened to a resolution of 9 μm and the central 2.5 mm was converted into an FE model through direct voxel conversion. Briefly, each voxel of the segmented image was converted into a linear hexahedral element with the corners of each voxel defining the nodes. A mesh convergence analysis of secondary osteonal bone demonstrated that the model was sufficiently converged at 10 μm [28]. Background voxels (i.e. pore space) were not converted

into corresponding elements. Elements were assigned homogenous, linear-elastic material properties with a modulus of 20 GPa and Poisson's ratio of 0.3 [29]. The boundary conditions of each model were consistent with experimental testing. A uniform compressive load was applied to the top surface and all nodes on the bottom surface were fixed in the vertical direction. The applied load corresponded to the experimental loading magnitude of each sample, equating to an apparent stress of either 60, 70, 80 or 90 MPa distributed over the entire cross-section. Stressed volume was calculated as the volume of elements experiencing a von Mises stress greater than the yield stress of cortical bone, which was assumed to be 108 MPa [30,31]. For an elastic modulus of 20 GPa, this yield stress corresponded to a strain magnitude of 5,400 $\mu\epsilon$. The von Mises failure criteria is based on the distortional energy in a material and may be an appropriate criterion to evaluate the shear failure that is typical of bone samples subjected to compressive loading.

Statistical analysis

Given that microarchitectural parameters illustrate considerable variation within the cross-section of a single bone [32], each sample was treated as an independent measure. The Shapiro-Wilk test of normality was used to evaluate the distribution of all experimental variables. Elastic modulus and mean Ca.Sp were normally distributed ($p \geq 0.265$), while apparent density, porosity, mean Ca.Dm, max Ca.Dm, stressed volume, and fatigue life were not ($p \leq 0.008$). Therefore, statistical differences amongst loading groups were examined using a Kruskal-Wallis non-parametric test. When evidence suggesting a difference in loading condition was observed, statistical analyses were followed with post-hoc pairwise comparisons with Bonferroni correction. The relationships between all log-transformed variables, including material properties, microarchitectural parameters, stressed volume, and fatigue life were examined using Pearson product-moment correlations. Statistical analyses regarding variable distribution and correlations were performed in SPSS (SPSS Inc., Chicago, IL, USA) with $\alpha = 0.05$.

A survival analysis was performed to assess the efficacy of stressed volume as a predictor of fatigue life. It was assumed that the variation in fatigue life could be adequately described using a log-normal accelerated failure time regression model in that the variability in log failure time could be explained by a model of the form:

$$\log T_i = \beta_0 + \beta_1 \log(x_i) + \gamma Z \quad (1)$$

where T_i is the failure time of sample i , β_0, β_1 are regression parameters, x_i was a predictive variable of interest, and Z was a random variable assumed to follow a standard normal distribution, scaled by factor γ [33]. Four models of the form in eq. 1 were fit where x_i was (a) the applied stress range, (b) normalized stress range (σ/E^*), (c) stressed volume, or (d) the ratio between stressed volume and bone volume for each sample. To account for the right censoring of the four samples that ran-out, samples parameter estimation was performed by maximum likelihood whereby uncensored samples contributed to the likelihood through their hazard function and censored samples via their survival function [33]. Model fitting was performed in R (v3.6.2, R Core Team, Austria) [34] using the 'survreg' function of the 'survival' package [35]. Model assumptions were validated graphically by a normal probability plot of model residuals against the Kaplan-Meier estimate for survival time and quantitatively through a Shapiro-Wilk test. The predictive performance of each model was assessed via the generalized adjusted R^2 measure.

RESULTS

The median and range of all dependent variables, both pooled data and within each loading group, is summarized in Table 2. There were no significant differences in any of the material properties

or microarchitectural parameters amongst loading groups ($p \geq 0.152$); however, the 90 MPa group demonstrated a significantly higher stressed volume and reduced fatigue life when compared to the 60 and 70 MPa loading groups. Figure 1 illustrates the distribution of stressed volume for representative samples in each loading group. It is clear that stressed volume was localized around vascular canals.

Fatigue-life measurements across loading groups ranged from 533 to 1,000,000 cycles, with four samples in the 60 MPa group reaching the run-out limit. Fatigue life was inversely related with porosity, mean Ca.Dm, and max Ca.Dm in all loading groups, while the relationship with mean Ca.Sp, max Ca.Sp, and Ca.N was not consistent across groups (see supplementary material). The degree of mineralization ($R^2 \leq 0.33$, $p \geq 0.108$) and heterogeneity ($R^2 \leq 0.27$, $p \geq 0.152$) were not significantly correlated with fatigue life, excluding the 60 MPa loading group in which a higher mean mineralization was associated with a longer fatigue life ($R^2 = 0.46$, $p = 0.045$). Stressed volume accounted for 67% of the observed variance in fatigue life ($p < 0.001$) and was a better predictor of fatigue life than either stress range ($R^2 = 0.49$, $p < 0.001$) or normalized stress range ($R^2 = 0.55$, $p < 0.001$; Figure 2). The likelihood of a sample surviving 10^4 cycles was approximately 25, 50, 80 and 100% when survival was predicted at stress ranges of 90, 80, 70, and 60 MPa, respectively (Figure 3). The median stressed volume for the 80 MPa group was three times smaller than that of the 90 MPa group and this corresponded to increases in the likelihood of a sample surviving 10^4 cycles by roughly 30%. This effect was not linear, as a similar three-fold reduction in stressed volume between the 70 and 60 MPa loading groups increased the likelihood of surviving 10^4 cycles approximately 10%.

Stressed volume was strongly correlated with porosity ($R^2 \geq 0.55$, $p \leq 0.022$) and maximum Ca.Dm ($R^2 \geq 0.59$, $p \leq 0.016$) in all loading groups, excluding 70 MPa (Figure 4a and 4c). Although not statistically significant, stressed volume in the 70 MPa group was moderately correlated with porosity ($R^2 \geq 0.43$, $p \leq 0.057$) and maximum Ca.Dm ($R^2 \geq 0.35$, $p \leq 0.09$). Mean Ca.Dm demonstrated a similar relationship with stressed volume for all loading groups, explaining 14-76% of the variance in stressed volume but was only significant within the 60 MPa ($R^2 = 0.53$, $p = 0.002$) and 90 MPa ($R^2 = 0.76$, $p = 0.026$) groups (Figure 4b). Both mean and maximum Ca.Sp were negatively correlated with stressed volume (Figure 4d and 4e); however, excluding maximum Ca.Sp in the 80 MPa loading group ($R^2 = 0.48$, $p = 0.04$), these correlations were weak and non-significant ($R^2 \leq 0.30$, $p \geq 0.09$). Ca.N was only related to the stressed volume within the 60 MPa group ($R^2 = 0.73$, $p = 0.003$), in which an increase in Ca.N was associated with a larger stressed volume (Figure 4f).

DISCUSSION

The fatigue life of cortical bone exhibits a large degree of scatter that is potentially due, in part, to the underlying microarchitecture. Vascular canals have been described as stress concentrators within the bone matrix, the magnitude and volume of which is dependent on canal morphology, and may act to reduce fatigue-life measurements [15,36]. The purpose of this study was two-fold; 1) to determine if stressed volume could predict the fatigue life of human cortical bone in zero-compression and 2) to establish the relationship between stressed volume and intracortical microarchitecture. Stressed volume was able to account for a majority of the scatter in fatigue-life measurements, and as expected, a larger stressed volume was associated with a shorter fatigue life. An increase in stressed volume was most strongly associated with higher levels of intracortical porosity and larger canal diameters. The findings from this study suggest that the fatigue life of human cortical bone in zero-compression is largely driven by intracortical microarchitecture, and that fatigue failure may be predicted by quantifying the stress concentrations associated with vascular canals.

Consistent with previous literature [7,8,37], stress range was a strong predictor of fatigue life, explaining nearly 50% of the observed scatter in fatigue-life measurement; normalizing stress range by elastic modulus explained an additional 6% of the observed scatter. Based on similar observations, Carter et al. [10] concluded that fatigue failure was governed by strain rather than stress range. Despite being loaded to the same stress magnitude, samples with lower elastic moduli will experience a higher initial strain. The elastic modulus of bone is dependent on mineral content and overall porosity [38]. Elastic modulus and intracortical porosity are inversely related, as bone that is more porous has a reduced effective cross-sectional area, and therefore a lower load-carrying capacity. In zero-tension, normalized stress range was strongly related to the rate of damage accumulation during fatigue testing [24,37]. Multiple regression analysis demonstrated that damage rate was primarily dependent on stress range, but including porosity increased the variance explained from 50 to 55% while mineral content had no effect [37]. We investigated the importance of mineral content post-hoc, by determining a tissue modulus for each sample that would be required to match FE-predicted apparent modulus with the experimental measurement. Tissue modulus was unable to account for a significant amount of the remaining variance in fatigue-life measurements. Taken together, these findings suggest that the reduced scatter associated normalized stress range is likely due to the influence of porosity on the elastic modulus and not from the contributions of mineral content.

While normalizing stress range by elastic modulus accounts for the reduced load-carrying capacity associated with increased porosity, it does not account for the influence of vascular canals as stress concentrators. Stressed volume, as quantified herein, reflects the peak magnitude and size of the stress concentrations, which are heavily influenced by the size, spatial distribution, density, and orientation of vascular canals [39,40]. In this study, stressed volume explained some 12% more variance in fatigue-life measurements than normalized stress range. Theoretically, it is possible to have bones of similar porosity but with different combinations of sizes and numbers of canals. Our findings suggest that a few large canals may be more detrimental to fatigue life than more abundant small canals, which is a distinction that porosity-based measurements are not be able to characterize. A larger stressed volume may reduce fatigue life as more of the bone volume is susceptible to developing new microcracks, and perhaps more importantly, a larger stressed volume will increase the likelihood of propagating pre-existing microcracks. Indeed, microcracks that initiate fracture are most often located near elevated porosity, suggesting that fracture may occur due to a single microcrack located within proximity of a canal [41].

Previous research has demonstrated an inverse relationship between intracortical porosity and the fatigue life of human bone [8,15]. These authors hypothesized that a shorter fatigue life associated with elevated porosity was related to the peak magnitude and size of the stress concentrations surrounding the vascular canals. Our findings support this hypothesis, as the stressed volume was localized to areas surrounding the vascular canals (Figure 1) and a larger stressed volume was strongly related to increased porosity and canal diameter. In general, increased stressed volume was also associated with smaller canal separation; however, this relationship was not consistent across loading groups. We speculate that the stress concentrations surrounding canals in close proximity may overlap and the superposition of these stress concentrations will cause elements that would otherwise be below yield to exceed the threshold of 108 MPa. Then again, if two canals are large enough to independently contribute to the stressed volume, this overlap would share elements of high stress and reduce the overall number of elements in the stressed volume calculation. These complex interactions may explain the inconsistent relationships observed between canal separation and stressed volume we observed. Porosity demonstrated the strongest and most consistent relationship with stressed

volume, likely because it is a composite measure of both canal diameter and canal number. It is important to acknowledge that, although not all parameters of microarchitecture were investigated in this study, all 3D structural information describing the vascular network are inherently captured in the FE models and is reflected in the measure of stressed volume.

After accounting for stressed volume, roughly 35% of the variance in fatigue life remained unexplained. We suspect this may be attributed to the dynamic process of fatigue failure and differences in material composition. The FE models only simulated the first loading cycle and did not characterize the development of microdamage or redistribution of stresses that would occur over multiple loading cycles. Under zero-compression, the fatigue behavior of bone exhibits a two-phase stiffness profile and may not display any indication of stiffness loss until the final 10% of its lifetime [42,43]. While a relatively constant stiffness profile provides some validity of using this quasi-static model to describe fatigue, the boundary conditions of the FE model and measure of stressed volume cannot account for the stochastic nature of crack propagation in the final stages of the fatigue life that ultimately lead to fatigue failure. The remaining scatter in fatigue-life measurements may also be explained by differences in the material composition including both the inorganic and organic components of bone. The collagen network governs the intrinsic toughening mechanisms that control crack initiation [44] and is expected to play a role in fatigue failure. Likewise, a more heterogeneous bone matrix may facilitate crack deflection, ultimately increasing the length of the crack trajectory and the fatigue resistance of bone [45]. As such, it was expected that more variance in grey scale values, a surrogate measure of heterogeneity, would be associated with a longer fatigue life; however, this relationship was weak and only observed at lower loading magnitudes.

The fatigue behavior of a material is typically characterized by a stress-life plot, which clearly demonstrates that small increases in loading magnitude may cause large reductions in the number of cycles to failure. This well-established stress-life relationship is the cornerstone of current approaches attempting to assess the risk of fatigue failure *in vivo* (i.e. stress fracture). Musculoskeletal FE models characterizing the mechanical loading environment of tibia have estimated a peak compressive stress ranging from 29.3-52.1 MPa and 89.7-146.3 MPa during walking [46–48] and running [3,4], respectively. Our findings indicate that a comparable increase from 60 and 90 MPa corresponds to a 98% reduction in the number of cycles to failure. While these changes in loading certainly have a marked effect on fatigue life and notable implications for predicting fatigue failure, smaller differences in estimated bone stress will be more difficult to interpret given the large degree of scatter within each load level. For example, Xu et al. [46] estimated that peak compressive tibial stress in subjects walking with and without a body-borne load equivalent to 30%BW were 58.5 and 40.3 MPa, respectively. Although a similar 20 MPa decrease in stress range (e.g. from 80 to 60 MPa) may increase the likelihood of surviving 10^5 cycles by more than 60% on average (Figure 3a), Figure 2a illustrates that fatigue-life measurements in the 60 and 80 MPa groups overlap by more than an order of magnitude. In other words, evaluating injury risk based on peak apparent bone stress alone may lead to inaccurate predictions of fatigue failure. The results of the present study suggest that incorporating microarchitectural features into computational assessments may provide better estimations of bone strength and fracture risk.

The image resolution used to quantify microarchitecture in this study is currently not possible *in vivo*. The best available technology is second generation high-resolution peripheral quantitative computed tomography (HR-pQCT), which can achieve an *in vivo* resolution as low as 61 μm [49]. Compared to synchrotron radiation micro-computed tomography (voxel resolution = 9 μm), HR-pQCT (voxel resolution=82 μm) underestimated cortical porosity by 6.7% on average but accurately detected pores larger than 140 μm in diameter [50]. Of the 36 samples imaged in the

current study, 20 samples had a maximum canal diameter greater than 140 μm , and the strong relationship between maximum canal diameter and stressed volume was dominated by canals larger than 120 μm (Figure 4). In this regard, current *in vivo* imaging technology may provide valuable information regarding large pores, which in this study were shown to have a marked influence on the mechanical fatigue behavior of cortical bone in zero-compression. In fact, it has been hypothesized that large resorption canals, a byproduct of bone remodelling in response to microdamage accumulation, may accelerate the development of fatigue fracture by inducing large stress concentrations. Resorption canals are four- to six-times larger than Haversian canals, on the order of 200-300 μm [51,52]. The results presented herein would suggest that, for a loading magnitude of 60 MPa, a 200 μm resorption canal may increase the stressed volume approximately 245% compared to a canal of 50 μm and ultimately reduce the fatigue life 2-3 orders of magnitude.

This study was limited to five donors and a relatively small sample size within each loading group. More donors are needed to confirm the generalizability of the present results. Bone samples were prepared both femoral and tibial mid-shafts and microarchitectural parameters may vary between these two bones [53]; however, we did not observe statistical differences in any microarchitectural parameters ($p \geq 0.168$) between bones, and hence all samples were pooled. While the samples were scanned as close to the fracture site as possible, the microarchitectural features and stressed volume quantified in the FE models did not correspond to the exact region of experimental fracture. A preliminary analysis of multiple sub-volumes within a given bone demonstrated coefficients of variation in microarchitectural parameters less than 7% and therefore the volume of interest was assumed to be representative of the whole sample. Furthermore, we would only expect measurements of microarchitecture and stressed volume at the fracture site to improve the correlations observed in this study. Discretizing the microarchitecture with a voxel-based mesh may cause stress discontinuities. A preliminary analysis demonstrated that stressed volume calculated using a geometric mesh may be 1-2.4% higher than that of a voxel-based mesh; however, the relationship between fatigue life and stressed volume was nearly identical using either a geometric or voxel-based mesh. While a voxel-based mesh may be acceptable to evaluate the relative relationship between stressed volume and fatigue life, a geometric mesh is likely required to obtain a more accurate estimate of stressed volume. To ensure that the relationship between fatigue life and stressed volume was not dependent on the chosen yield stress threshold, a sensitivity analysis was performed (see supplementary material) in which stressed volume was calculated using yield stress thresholds between 100-120 MPa. The correlation between stressed volume and fatigue life was unaffected by changes in yield stress, with the weakest and strongest correlations varying by less than 3% ($R^2 = 0.653$ at 100 MPa and $R^2 = 0.677$ at 115 MPa).

To summarize, this study utilized a combination of experimental fatigue testing, X-ray microscopy and FE modeling to establish the relationship between the stressed volume associated with vascular canals and the fatigue life of human cortical bone in zero-compression. Stressed volume was a better predictor of fatigue life than both stress range and normalized stress range, accounting for 67% of the variance in fatigue-life measurements. Stressed volume was most strongly correlated with maximum canal diameter, indicating the important influence that feature size has on the peak magnitude and size of the stress concentration within bone. We suspect that a larger stressed volume increases the likelihood of encountering and propagating pre-existing microcracks, thereby leading to a reduction in fatigue life.

ACKNOWLEDGMENTS

This work was supported in part by a seed grant from the Faculty of Kinesiology at the University of Calgary as well as the Natural Science and Engineering Research Council of Canada (Grant Nos. NSERC; RGPIN 01029–2015 and RTI 00013–2016).

REFERENCES

- [1] D.B. Burr, C.H. Turner, P. Naick, M.R. Forwood, W. Ambrosius, M.S. Hasan, R. Pidaparti, Does microdamage accumulation affect the mechanical properties of bone?, *J. Biomech.* 31 (1998) 337–345. [https://doi.org/10.1016/S0021-9290\(98\)00016-5](https://doi.org/10.1016/S0021-9290(98)00016-5).
- [2] D.B. Burr, C. Milgrom, R.D. Boyd, W.L. Higgins, G. Robin, E.L. Radin, Experimental stress fractures of the tibia, *J. Bone Jt. Surgery, Br. Vol.* 72 (1990) 370–375.
- [3] S.A. Meardon, J.D. Willson, S.R. Gries, T.W. Kernozek, T.R. Derrick, Bone stress in runners with tibial stress fracture, *Clin. Biomech.* 30 (2015) 895–902. <https://doi.org/10.1016/j.clinbiomech.2015.07.012>.
- [4] C. Xu, A. Silder, J. Zhang, J. Reifman, G. Unnikrishnan, A cross-sectional study of the effects of load carriage on running characteristics and tibial mechanical stress: implications for stress-fracture injuries in women, *BMC Musculoskelet. Disord.* 18 (2017) 1–12. <https://doi.org/10.1186/s12891-017-1481-9>.
- [5] D. Taylor, F.J. O'Brien, A. Prina-mello, C. Ryan, P. O'Reilly, T.C. Lee, Compression data on bovine bone confirms that a “stressed volume” principle explains the variability of fatigue strength results, *J. Biomech.* 32 (1999) 1199–1203.
- [6] D.R. Carter, W.E. Caler, D.M. Spengler, V.H. Frankel, Fatigue behavior of adult cortical bone: the influence of mean strain and strain range., *Acta Orthop. Scand.* 52 (1981) 481–490. <https://doi.org/10.3109/17453678108992136>.
- [7] D.R. Carter, W.C. Hayes, Fatigue life of compact bone-I: Effects of stress amplitude, temperature and density, *J. Biomech.* 9 (1976) 27–34.
- [8] P. Zioupos, M. Gresle, K. Winwood, Fatigue strength of human cortical bone: Age, physical, and material heterogeneity effects, *J. Biomed. Mater. Res. - Part A.* 86 (2007) 627–636. <https://doi.org/10.1002/jbm.a.31576>.
- [9] V.A. Gibson, S.M. Stover, J.C. Gibeling, S.J. Hazelwood, R.B. Martin, Osteonal effects on elastic modulus and fatigue life in equine bone, *J. Biomech.* 39 (2006) 217–225. <https://doi.org/10.1016/j.jbiomech.2004.12.002>.
- [10] D.R. Carter, W.E. Caler, D.M. Spengler, V.H. Frankel, Uniaxial fatigue of human cortical bone. The influence of tissue physical characteristics, *J. Biomech.* 14 (1981) 461–470. [https://doi.org/10.1016/0021-9290\(81\)90096-8](https://doi.org/10.1016/0021-9290(81)90096-8).
- [11] M.B. Schaffler, E.L. Radin, D.B. Burr, Mechanical and Morphological Effects of Strain Rate on Fatigue of Compact Bone, *Bone.* 10 (1989) 207–214.
- [12] L.L. Loundagin, T.A. Schmidt, W.B. Edwards, Mechanical Fatigue of Bovine Cortical Bone Using Ground Reaction Force Waveforms in Running, *J. Biomech. Eng.* 140 (2018). <https://doi.org/10.1115/1.4038288>.
- [13] D.R. Carter, W.C. Hayes, D.J. Schurman, Fatigue life of compact bone-II: effects of microstructure and density, *J. Biomech.* 9 (1976) 211–218.
- [14] F.G. Evans, M.L. Riolo, Relations between the Fatigue Life and Histology of Adult Human Cortical Bone, *J. Bone Jt. Surg.* 52 (1970) 1579–1586.
- [15] L.L. Loundagin, I.T. Haider, D.M.L. Cooper, W.B. Edwards, Association between intracortical microarchitecture and the compressive fatigue life of human bone: A pilot study, *Bone Reports.* 12 (2020) 100254. <https://doi.org/10.1016/j.bonr.2020.100254>.
- [16] M.E. Launey, M.J. Buehler, R.O. Ritchie, On the Mechanistic Origins of Toughness in Bone, 2010. <https://doi.org/10.1146/annurev-matsci-070909-104427>.
- [17] R.K. Nalla, J.S. Stölken, J.H. Kinney, R.O. Ritchie, Fracture in human cortical bone: Local fracture criteria and toughening mechanisms, *J. Biomech.* 38 (2005) 1517–1525. <https://doi.org/10.1016/j.jbiomech.2004.07.010>.
- [18] G.C. Reilly, Observations of microdamage around osteocyte lacunae in bone, *J. Biomech.* 33 (2000) 1131–1134. [https://doi.org/10.1016/S0021-9290\(00\)00090-7](https://doi.org/10.1016/S0021-9290(00)00090-7).
- [19] D.R. Carter, W.C. Hayes, Compact bone fatigue damage: A microscopic examination, *Clin. Orthop. Relat. Res.* 127 (1977) 265–274.

- [20] S. Suresh, *Fatigue of Materials*, 2nd ed., Cambridge University Press, New York, NY, 1998.
- [21] D. Taylor, The theory of critical distances, *Eng. Fract. Mech.* 75 (2008) 1696–1705. <https://doi.org/10.1016/j.engfracmech.2007.04.007>.
- [22] D. Taylor, Analysis of fatigue failures in components using the theory of critical distances, *Eng. Fail. Anal.* 12 (2005) 906–914. <https://doi.org/10.1016/j.engfailanal.2004.12.007>.
- [23] D. Taylor, Geometrical effects in fatigue : a unifying theoretical model, *Int. J. Fatigue.* 21 (1999) 413–420.
- [24] J.R. Cotton, K. Winwood, P. Zioupos, M. Taylor, Damage rate is a predictor of fatigue life and creep strain rate in tensile fatigue of human cortical bone samples., *J. Biomech. Eng.* 127 (2005) 213–219. <https://doi.org/10.1115/1.1865188>.
- [25] D.R. Carter, W.E. Caler, A Cumulative Damage Model for Bone Fracture, *J. Orthop. Res.* 3 (1985) 84–90.
- [26] J. Schindelin, I. Arganda-Carreras, E. Frise, V. Kaynig, M. Longair, T. Pietzsch, S. Preibisch, C. Rueden, S. Saalfeld, B. Schmid, J.-Y. Tinevez, D.J. White, V. Hartenstein, K. Eliceiri, P. Tomancak, A. Cardona, Fiji - an Open Source platform for biological image analysis, *Nat. Methods.* 9 (2012) 676–82. <https://doi.org/10.1038/nmeth.2019.Fiji>.
- [27] M. Doube, M.M. Kłosowski, I. Arganda-carreras, P. Fabrice, BoneJ : free and extensible bone image analysis in ImageJ, *Bone.* 47 (2010) 1076–1079. <https://doi.org/10.1016/j.bone.2010.08.023.BoneJ>.
- [28] L.L. Loundagin, W.B. Edwards, Stressed volume around vascular canals explains compressive fatigue life variation of secondary osteonal bone but not plexiform bone, *J. Mech. Behav. Biomed. Mater.* 111 (2020) 104002. <https://doi.org/10.1016/j.jmbbm.2020.104002>.
- [29] S.C. Cowin, *Bone Mechanics Handbook*, CRC Press LLC, 2001.
- [30] H. Leng, X.N. Dong, X. Wang, Progressive post-yield behavior of human cortical bone in compression for middle-aged and elderly groups, *J. Biomech.* (2009). <https://doi.org/10.1016/j.jbiomech.2008.11.016>.
- [31] X.N. Dong, R.L. Acuna, Q. Luo, X. Wang, Orientation dependence of progressive post-yield behavior of human cortical bone in compression, *J. Biomech.* (2012). <https://doi.org/10.1016/j.jbiomech.2012.08.034>.
- [32] D.M.L. Cooper, a L. Turinsky, C.W. Sensen, B. Hallgrímsson, Quantitative 3D analysis of the canal network in cortical bone by micro-computed tomography., *Anat. Rec.* 274 (2003) 169–179. <https://doi.org/10.1002/ar.b.10024>.
- [33] J.F. Lawless, *Statistical Model and Methods for Lifetime Data*, 2nd ed., John Wiley & Sons Inc., Hoboken, NJ, 2003.
- [34] R Core Team, *R: A language and environment for statistical computing*. R Foundation for Statistical Computing, (2017).
- [35] T.M. Therneau, *A Package for Survival Analysis in R*, (2020).
- [36] J.D. Currey, Stress concentrations in bone, *Q. J. Microsc. Sci.* 103 (1962) 111–133. <https://doi.org/10.1007/BF02326000>.
- [37] P. Zioupos, X.T. Wang, J.D. Currey, The accumulation of fatigue microdamage in human cortical bone of two different ages in vitro, *Clin. Biomech.* 11 (1996) 365–375. [https://doi.org/10.1016/0268-0033\(96\)00010-1](https://doi.org/10.1016/0268-0033(96)00010-1).
- [38] M.B. Schaffler, D.B. Burr, Stiffness of Compact-Bone: Effects of Porosity and Density, *J. Biomech.* 21 (1988) 13–16. [https://doi.org/10.1016/0021-9290\(88\)90186-8](https://doi.org/10.1016/0021-9290(88)90186-8).
- [39] T. Davis, D. Healy, A. Bubeck, R. Walker, Stress concentrations around voids in three dimensions : The roots of failure, *J. Struct. Geol.* 102 (2017) 193–207. <https://doi.org/10.1016/j.jsg.2017.07.013>.
- [40] D.A. Hoey, D. Taylor, Quantitative analysis of the effect of porosity on the fatigue strength of bone cement, *Acta Biomater.* 5 (2009) 719–726.

- <https://doi.org/10.1016/j.actbio.2008.08.024>.
- [41] T.L. Turnbull, A.P. Baumann, R.K. Roeder, Fatigue microcracks that initiate fracture are located near elevated intracortical porosity but not elevated mineralization, *J. Biomech.* 47 (2014) 3135–3142. <https://doi.org/10.1016/j.jbiomech.2014.06.022>.
- [42] C.A. Pattin, W.E. Caler, D.R. Carter, Cyclic mechanical property degradation during fatigue loading of cortical bone, *J. Biomech.* 29 (1996) 69–79. [https://doi.org/10.1016/0021-9290\(94\)00156-1](https://doi.org/10.1016/0021-9290(94)00156-1).
- [43] W.T. George, D. Vashishth, Damage mechanisms and failure modes of cortical bone under components of physiological loading, *J. Orthop. Res.* 23 (2005) 1047–1053. <https://doi.org/10.1016/j.orthres.2005.02.008>.
- [44] R.O. Ritchie, M.J. Buehler, P. Hansma, Plasticity and toughness in bone, *Phys. Today.* 62 (2009) 41–47. <https://doi.org/10.1063/1.3156332>.
- [45] O.L. Katsamenis, T. Jenkins, P.J. Thurner, Toughness and damage susceptibility in human cortical bone is proportional to mechanical inhomogeneity at the osteonal-level, *Bone.* 76 (2015) 158–168. <https://doi.org/10.1016/j.bone.2015.03.020>.
- [46] C. Xu, A. Silder, J. Zhang, J. Hughes, G. Unnikrishnan, J. Reifman, V. Rakesh, An Integrated Musculoskeletal-Finite-Element Model to Evaluate Effects of Load Carriage on the Tibia during Walking, *J. Biomech. Eng.* 138 (2016) 1–11. <https://doi.org/10.1115/1.4034216>.
- [47] C. Xu, J. Reifman, M. Baggaley, W.B. Edwards, G. Unnikrishnan, Individual Differences in Women during Walking Affect Tibial Response to Load Carriage: The Importance of Individualized Musculoskeletal Finite-Element Models, *IEEE Trans. Biomed. Eng.* 67 (2020) 545–555. <https://doi.org/10.1109/TBME.2019.2917415>.
- [48] T.R. Derrick, W.B. Edwards, R.E. Fellin, J.F. Seay, An integrative modeling approach for the efficient estimation of cross sectional tibial stresses during locomotion, *J. Biomech.* 49 (2016) 429–435. <https://doi.org/10.1016/j.jbiomech.2016.01.003>.
- [49] S.L. Manske, E.M. Davison, L.A. Burt, D.A. Raymond, S.K. Boyd, The Estimation of Second-Generation HR-pQCT From First-generation HR-pQCT Using In Vivo Cross-Calibration, *J. Bone Miner. Res.* 32 (2017) 1514–1524. <https://doi.org/10.1002/jbmr.3128>.
- [50] B.L. Jorgenson, H.R. Buie, D.D. McErlain, C. Sandino, S.K. Boyd, A comparison of methods for in vivo assessment of cortical porosity in the human appendicular skeleton, *Bone.* 73 (2015) 167–175. <https://doi.org/10.1016/j.bone.2014.11.023>.
- [51] K.L. Bell, N. Loveridge, J. Power, N. Garrahan, B.F. Meggitt, J. Reeve, Regional differences in cortical porosity in the fractured femoral neck, *Bone.* 24 (1999) 57–64. [https://doi.org/10.1016/S8756-3282\(98\)00143-4](https://doi.org/10.1016/S8756-3282(98)00143-4).
- [52] G.R. Jordan, N. Loveridge, K.L. Bell, J. Power, N. Rushton, J. Reeve, Spatial clustering of remodeling osteons in the femoral neck cortex: A cause of weakness in hip fracture?, *Bone.* 26 (2000) 305–313. [https://doi.org/10.1016/S8756-3282\(99\)00272-0](https://doi.org/10.1016/S8756-3282(99)00272-0).
- [53] Y.N. Yeni, C.U. Brown, Z. Wang, T.L. Norman, The influence of bone morphology on fracture toughness of the human femur and tibia, *Bone.* 21 (1997) 453–459. [https://doi.org/10.1016/S8756-3282\(97\)00173-7](https://doi.org/10.1016/S8756-3282(97)00173-7).
- [54] B. Efron, R. Tibshirani, Bootstrap Methods for Standard Errors, Confidence Intervals, and Other Measures of Statistical Accuracy, *Stat. Sci.* 1 (1986) 54–77. <https://doi.org/10.1214/ss/1177013437>.

FIGURES

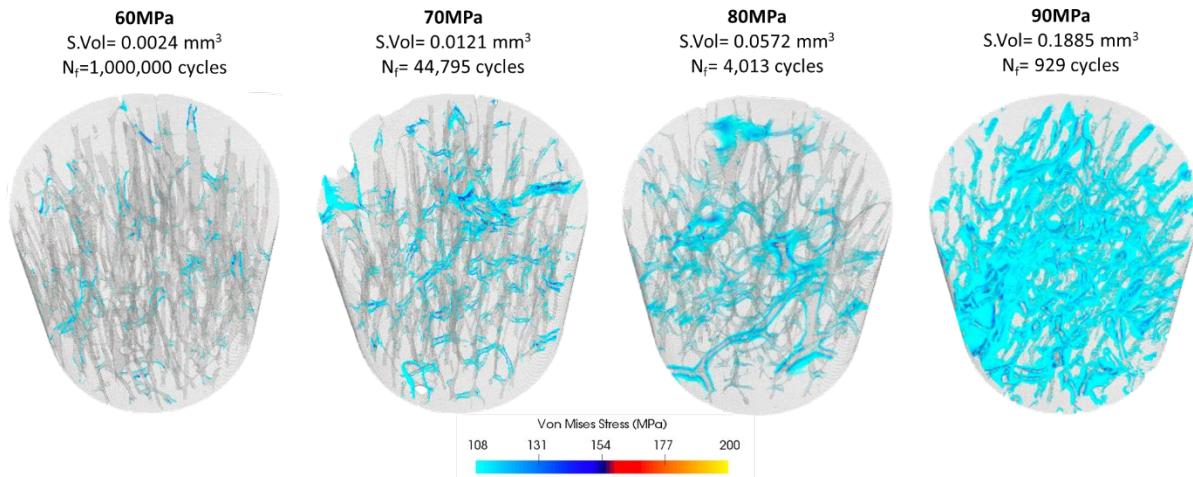


Figure 1: The stressed volume in a representative sample from each loading group. The highlighted volume is the volume of material above the yield threshold of 108MPa.

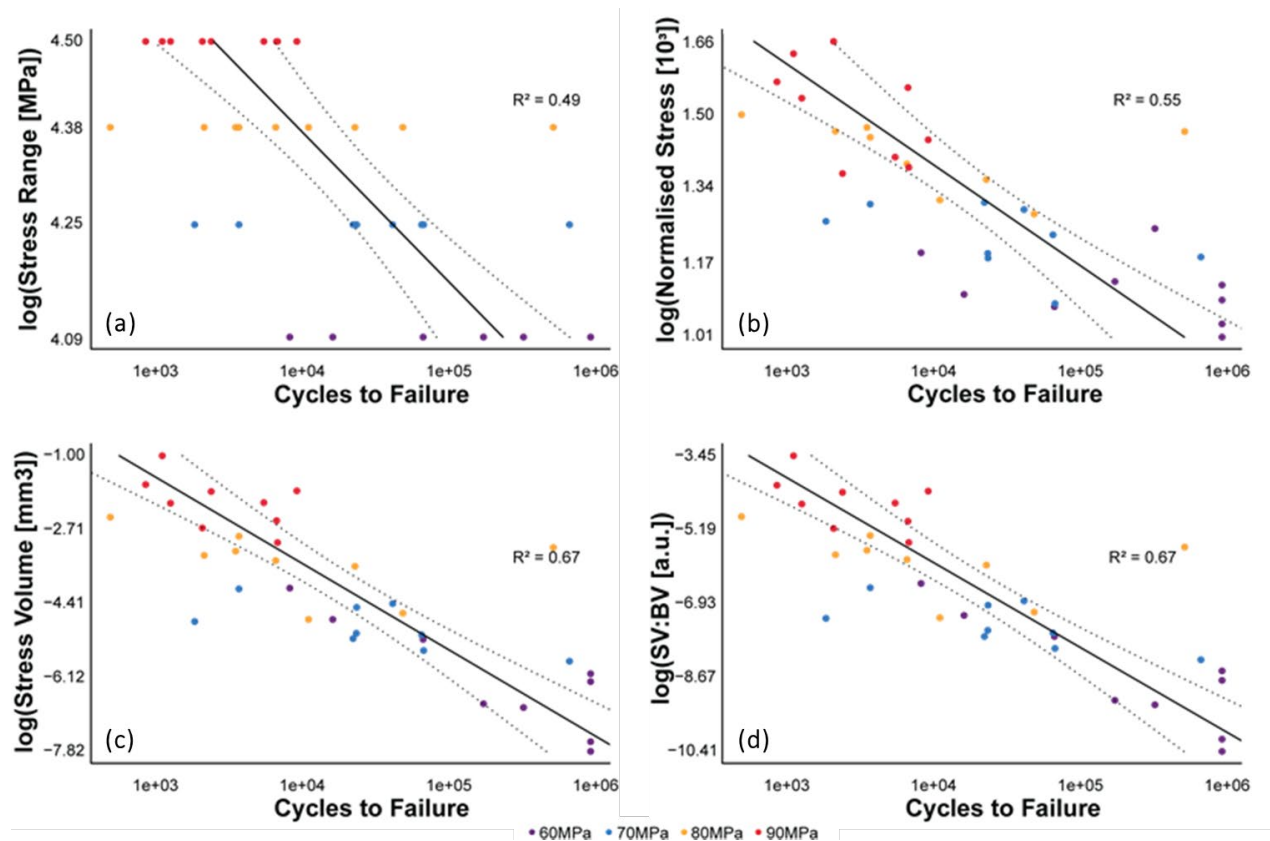


Figure 2: Relationship between fatigue life and a) stress range, b) normalized stress range (σ/E^*), c) stressed volume, and d) stressed volume to total bone volume ratio (SV:BV). The relationship between cycles to failure and the SV:BV ratio is identical to the absolute stressed volume and is provided for the reader's convenience to demonstrate the

stressed volume relative to the sample volume. 95% confidence intervals for the mean predicted failure time are indicated by dotted lines.

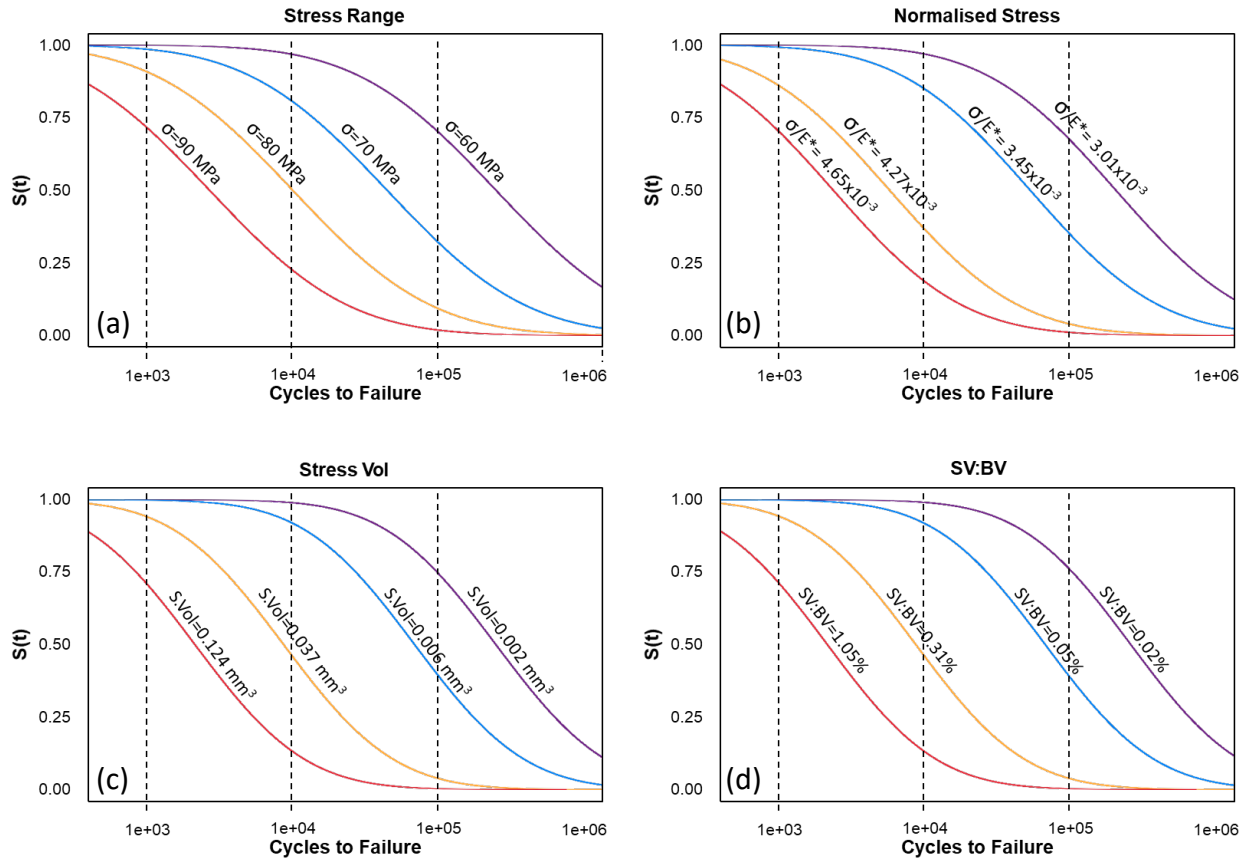


Figure 3: The likelihood of survival as a function of (a) stress range, (b) normalized stress range (σ/E^*), (c) stressed volume and (d) the stressed volume to total bone volume ratio (SV:BV). The relationship between the likelihood of survival and the SV:BV ratio is identical to the absolute stressed volume and is provided for the reader's convenience to demonstrate the stressed volume relative to the sample volume.

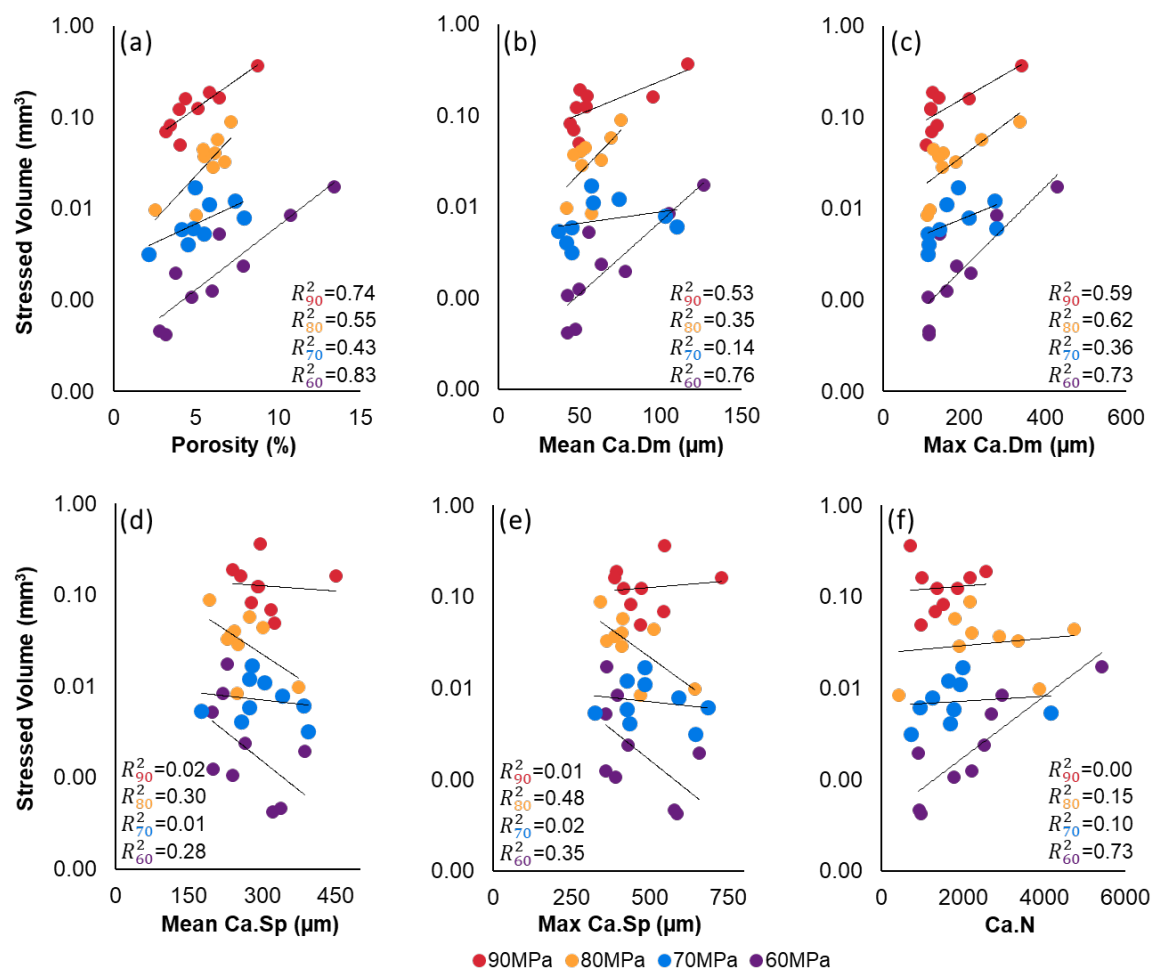


Figure 4: Relationships between all microarchitectural parameters and the stressed volume (log scale) within each loading group.

TABLES

Table 1: Demographic information for the five donors and the number of samples obtained from each donor.

Donor	1	2	3	4	5
Age	85	77	68	58	46
Sex	Female	Male	Male	Female	Male
Height (cm)	172	173	174	165	182
Weight (kg)	58.5	67.7	81.0	80.4	95.2
Cause of Death	Congestive heart failure	Chronic obstructive pulmonary disease	Traumatic brain injury	Cardiac arrest	Cardiac event
N	10	11	6	5	4

Table 2: Median and range (min-max) of all material properties, microarchitectural parameters, stressed volume, and fatigue life of all samples (combined) and within in each loading group (*statistically different from the 90MPa group, b= statistically different from the 80MPa group p≤0.05).

	Combined (n=36)		60MPa (n=9)		70MPa (n=9)		80MPa (n=9)		90MPa (n=9)	
	Median	(Min-Max)	Median	(Min-Max)	Median	(Min-Max)	Median	(Min-Max)	Median	(Min-Max)
Density(g/cm³)	1.91	(1.45-2.05)	1.92	(1.45-1.95)	1.92	(1.77-2.05)	1.90	(1.83-2.05)	1.91	(1.81-2.02)
Modulus (GPa)	19.83	(17.05-23.73)	19.93	(17.22-21.91)	20.37	(18.96-23.73)	18.75	(17.83-22.23)	19.34	(17.05-22.86)
Porosity(%)	5.45	(2.15-13.40)	5.97	(2.81-13.40)	4.94	(2.15-7.90)	6.06	(2.54-7.15)	4.37	(3.21-8.74)
Mean Ca.Dm (µm)	54.09	(37.11-126.77)	56.02	(42.60-126.77)	57.45	(37.11-110.08)	53.95	(42.38-75.89)	50.19	(44.50-117.10)
Max Ca.Dm (µm)	139.67	(106.31-430.67)	157.58	(111.6-430.67)	155.50	(111.08-280.44)	147.37	(108.28-336.97)	122.91	(106.31-341.68)
Mean Ca.Sp (µm)	273.50	(175.61-449.60)	238.95	(197.97-387.66)	288.62	(175.61-393.57)	242.30	(193.13-273.50)	293.04	(239.82-449.60)
Max Ca.Sp (µm)	427.44	(323.71-729.21)	396.90	(357.83-657.58)	458.95	(323.71-683.94)	410.56	(341.06-471.28)	471.24	(386.79-729.21)
Ca.N	1840	(427-5436)	2217	(903-5436)	1676	(712-4170)	2225	(427-4747)	1374	(715-2566)
S.Vol (mm³)	0.0146	(0.0004-0.3663)	0.0020 ^a	(0.0004-0.0173)	0.0061 ^a	(0.0032-0.0170)	0.0368	(0.0084-0.0889)	0.1243	(0.0494-0.3663)
Nf (cycles)	14726	(533-1000000)	348972 ^{a,b}	(8910-1000000)	25465 ^a	(2004-717968)	7146	(533-556759)	2598	(929-9962)

SUPPLEMENTARY MATERIAL

Sensitivity of the assumed yield stress

A sensitivity analysis was performed to confirm that the relationship between fatigue life and stressed volume was not dependent on the chosen yield stress threshold. In addition to the presented yield stress threshold of 108MPa, the stressed volume of each sample was calculated using 5 additional yield stress thresholds between 100-120 MPa at 5 MPa increments (Table S1). A lower yield stress resulted in a larger stress volume and the stressed volume was highly correlated with the given yield stress threshold ($R^2 = 0.99$). More importantly, the correlation between stressed volume and fatigue life was unaffected by changes in yield stress. The yield stress (108 MPa) used for the formal analysis presented in the manuscript demonstrated the second strongest relationship with fatigue life; however, there was remarkably little variation, less than 3%, between even the weakest and strongest correlations ($R^2 = 0.653$ at 100 MPa and $R^2 = 0.677$ at 115 MPa).

Table S1: Results of the survival analysis model of stressed volume as a predictor of fatigue life when stressed volume was calculated using a range of yield stress thresholds. The stressed volume calculated from all thresholds predicted a significant amount of variance in the fatigue life. A 95% confidence interval for R^2 was obtained using a nonparametric bootstrap procedure with 10,000 bootstrap replicates [54].

Yield Stress Threshold (MPa)	β	SE(β)	AIC	R^2_{adj}	R^2 CI	p-value
100	-1.07	0.136	732.62	0.653	(0.433, 0.819)	≤ 0.001
105	-1.139	0.141	730.93	0.669	(0.445, 0.843)	≤ 0.001
108	-1.155	0.143	730.7	0.671	(0.440, 0.843)	≤ 0.001
110	-1.157	0.143	730.44	0.673	(0.429, 0.839)	≤ 0.001
115	-1.135	0.141	730.02	0.677	(0.445, 0.849)	≤ 0.001
120	-1.123	0.141	730.85	0.669	(0.413, 0.850)	≤ 0.001

Influence of microarchitecture on fatigue life

Porosity is a function of both the abundance and size of canals. The results of this study suggest that the reduced fatigue life associated with increased porosity can be attributed to larger canals rather than more numerous canals. Porosity was inversely related with fatigue life in all loading groups; however, only the 60 ($R^2=0.76$, $p=0.002$) and 70 MPa ($R^2=0.54$, $p=0.024$) loading groups reached significance. Similarly, all groups demonstrated that an increase in mean Ca.Dm and max Ca.Dm resulted in a shorter fatigue life, but this relationship was only significant in the 60 MPa loading group ($R^2 \geq 0.57$, $p \leq 0.018$). The relationship between Ca.N and fatigue life is less clear. Excluding the 60 MPa group ($R^2=0.75$, $p=0.003$), the correlations between Ca.N and fatigue life were weak, non-significant, and inconsistent across loading groups ($R^2 \leq 0.31$, $p \geq 0.12$).

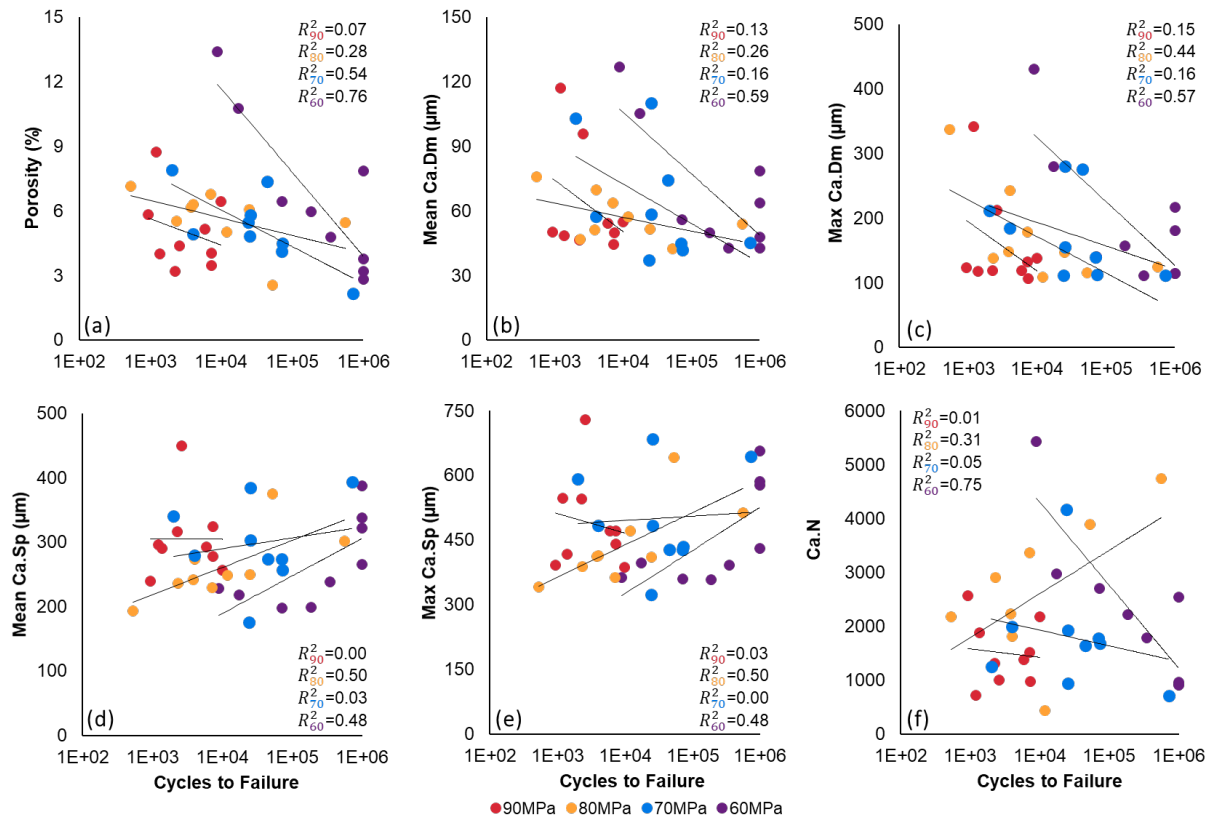


Figure S1: Relationships between all microarchitectural parameters and fatigue life (log scale) within each loading group examined using Pearson product-moment correlations.